The Astrophysical Journal Letters, 951:L17 (11pp), 2023 July 1 https://doi.org/10.3847/2041-8213/acd938
© 2023. The Author(s). Published by the American Astronomical Society.
OPEN ACCESS

Early Results from GLASS–JWST. XXI. Rapid Asembly of a Galaxy at $z = 6.23$ Revealed by Its C/O Abundance

Tucker Jones[1], Ryan Sanders[1,21], Yuguang Chen[1], Xin Wang[2,3,4], Takahiro Morishita[5], Guido Roberts-Borsani[6], Tommaso Treu[6], Alan Dressler[7], Emiliano Merlin[8], Diego Paris[8], Paola Santini[8], Pietro Bergamini[9,10], A. Henry[11,12], Erin Huntzinger[1], Themiya Nanayakkara[13], Kristan Boyett[14,15], Marusa Bradac[1,16], Gabriel Brammer[17,18], Antonello Calabró[8], Karl Glazebrook[13], Kathryn Grasha[15,19,22], Sara Mascia[8], Laura Pentericci[8], Michele Trenti[14,15], and Benedetta Vulcani[20]

[1] Department of Physics and Astronomy, University of California Davis, 1 Shields Avenue, Davis, CA 95616, USA; tdjones@ucdavis.edu
[2] School of Astronomy and Space Science, University of Chinese Academy of Sciences (UCAS), Beijing 100049, People's Republic of China
[3] National Astronomical Observatories, Chinese Academy of Sciences, Beijing 100101, People's Republic of China
[4] Institute for Frontiers in Astronomy and Astrophysics, Beijing Normal University, Beijing 102206, People's Republic of China
[5] Infrared Processing and Analysis Center, Caltech, 1200 E. California Blvd., Pasadena, CA 91125, USA
[6] Department of Physics and Astronomy, University of California, Los Angeles, 430 Portola Plaza, Los Angeles, CA 90095, USA
[7] The Observatories, The Carnegie Institution for Science, 813 Santa Barbara St., Pasadena, CA 91101, USA
[8] INAF Osservatorio Astronomico di Roma, Via Frascati 33, I-00078 Monteporzio Catone, Rome, Italy
[9] Dipartimento di Fisica, Università degli Studi di Milano, Via Celoria 16, I-20133 Milano, Italy
[10] INAF - OAS, Osservatorio di Astrofisica e Scienza dello Spazio di Bologna, via Gobetti 93/3, I-40129 Bologna, Italy
[11] Space Telescope Science Institute, 3700 San Martin Drive, Baltimore, MD 21218, USA
[12] Center for Astrophysical Sciences, Department of Physics and Astronomy, Johns Hopkins University, Baltimore, MD 21218, USA
[13] Centre for Astrophysics and Supercomputing, Swinburne University of Technology, PO Box 218, Hawthorn, VIC 3122, Australia
[14] School of Physics, University of Melbourne, Parkville 3010, VIC, Australia
[15] ARC Centre of Excellence for All Sky Astrophysics in 3 Dimensions (ASTRO 3D), Australia
[16] University of Ljubljana, Department of Mathematics and Physics, Jadranska ulica 19, SI-1000 Ljubljana, Slovenia
[17] Cosmic Dawn Center (DAWN), Denmark
[18] Niels Bohr Institute, University of Copenhagen, Jagtvej 128, DK-2200 Copenhagen N, Denmark
[19] Research School of Astronomy and Astrophysics, Australian National University, Canberra, ACT 2611, Australia
[20] INAF- Osservatorio astronomico di Padova, Vicolo Osservatorio 5, I-35122 Padova, Italy
Received 2023 January 17; revised 2023 April 29; accepted 2023 May 11; published 2023 July 3

Abstract

The abundance of carbon relative to oxygen (C/O) is a promising probe of star formation history in the early universe, as the ratio changes with time due to production of these elements by different nucleosynthesis pathways. We present a measurement of $\log(\mathrm{C/O}) = -1.01 \pm 0.12$ (stat) ± 0.15 (sys) in a $z = 6.23$ galaxy observed as part of the GLASS–JWST Early Release Science Program. Notably, we achieve good precision thanks to the detection of the rest-frame ultraviolet O III], C III], and C IV emission lines delivered by JWST/NIRSpec. The C/O abundance is ∼0.8 dex lower than the solar value and is consistent with the expected yield from core-collapse supernovae, indicating that longer-lived intermediate-mass stars have not fully contributed to carbon enrichment. This in turn implies rapid buildup of a young stellar population with age $\lesssim$100 Myr in a galaxy seen ∼900 Myr after the big bang. Our chemical abundance analysis is consistent with spectral energy distribution modeling of JWST/NIRCam photometric data, which indicates a current stellar mass $\log M_*/M_\odot = 8.4^{+0.4}_{-0.2}$ and specific star formation rate $\simeq$20 Gyr^{-1}. These results showcase the value of chemical abundances and C/O in particular to study the earliest stages of galaxy assembly.

Unified Astronomy Thesaurus concepts: High-redshift galaxies (734); Galaxy abundances (574); Abundance ratios (11); Emission line galaxies (459)

1. Introduction

The abundance of heavy elements is a fundamental property of galaxies that traces their growth and star formation, since metals originate from nucleosynthesis in the stellar evolution process (e.g., Matteucci 2012; Maiolino & Mannucci 2019). The abundance pattern of metals with different nucleosynthetic origins and enrichment timescales provides a particularly powerful tool for constraining the formation history of galaxies. Since different elements can originate from stars of different masses, the timescales on which the interstellar medium (ISM) is enriched with these elements will differ according to the variation of stellar lifetime with mass. In the simple "closed-box" chemical evolution model, oxygen and other α elements are predominantly produced in massive stars ($M \gtrsim 8\,M_\odot$) and returned to the ISM on short timescales by core-collapse supernovae (SNe; ∼10 Myr). While carbon is also produced in massive stars, another important pathway is via intermediate-mass ($M \sim 1$–$4\,M_\odot$) asymptotic giant branch (AGB) stars with lifetimes of ∼100 Myr–10 Gyr (e.g., Kobayashi et al. 2011, 2020). Consequently, galaxies with a formation timescale of $\lesssim$100 Myr will have C/O abundance approximately equivalent to the yield from core-collapse SNe alone, while

[21] NHFP Hubble Fellow.
[22] ARC DECRA Fellow.

Original content from this work may be used under the terms of the Creative Commons Attribution 4.0 licence. Any further distribution of this work must maintain attribution to the author(s) and the title of the work, journal citation and DOI.

C/O increases at ages $\gtrsim$100 Myr. The gas-phase abundance ratio C/O can thus indicate whether the stellar population in a galaxy is dominated by stars younger or older than ∼100 Myr.

C/O abundance is a promising tracer of the earliest phases of galaxy formation both because of its variation on relatively short timescales (∼100 Myr) and because it can be derived from ratios of rest-frame ultraviolet (UV) emission lines of C (C III] λλ1907,1909, C IV λλ1548,1550) and O (O III] λλ1661,1666). These are typically the brightest UV nebular emission lines (e.g., Byler et al. 2018; Berg et al. 2022) and are accessible with JWST/NIRSpec out to extremely high redshifts ($z \sim 4$–30). These lines have a further advantage that their ratios are relatively insensitive to dust reddening due to their close proximity in wavelength. Measurements of C III], C IV, and O III] at $z > 6$ have shown that these high-ionization lines are strong in $z > 6$ sources, with equivalent widths significantly larger than all but the most extreme galaxies at $z \sim 0$ (e.g., Stark et al. 2015a, 2015b, 2017; Mainali et al. 2017; Senchyna et al. 2017; Hutchison et al. 2019). The C/O abundance ratio is thus a premier tool for inferring the formation timescales of galaxies in the epoch of reionization during the first billion years of cosmic history.

In the local universe, a relation has been found between C/O and O/H in which C/O plateaus to a low-metallicity floor which averages log(C/O)∼ −0.7 at 12+log(O/H)<8.0, the primary nucleosynthesis regime, while C/O increases with O/H at higher metallicity (e.g., Henry et al. 2000; Esteban et al. 2014; Berg et al. 2016, 2019; Toribio San Cipriano et al. 2017). Using rest-UV spectroscopy of nearby dwarf galaxies, Berg et al. (2019) showed that this relation displays a large intrinsic scatter of ∼0.2 dex in C/O at fixed O/H. This scatter has been shown to be a function of the star formation history (SFH) (for the enrichment timescale reasons outlined above) and the preferential removal of O relative to C by SNe-driven outflows, where galaxies with shorter formation timescales and little preferential O removal have lower C/O (Yin et al. 2011; Berg et al. 2019). Intermediate-redshift galaxies at $z \sim 2$–3 fall on the low-metallicity plateau with a mean value and scatter similar to the $z \sim 0$ sample (e.g., Berg et al. 2018, 2019). Arellano-Córdova et al. (2022) recently reported the first C/O determination at $z > 6$ enabled by JWST spectroscopy. These authors found log(C/O) $= -0.83 \pm 0.38$ for a $z = 8.495$ galaxy, consistent with the local low-metallicity plateau. However, the interpretation of this value is clouded by its low precision due to a marginal detection of C III] (2.4σ) and no detection of rest-UV O III], relying instead on the ratio relative to rest-optical [O III] lines that is highly sensitive to dust reddening. This early result nonetheless provides a precise O/H abundance and shows the promise of JWST spectroscopy for abundance patterns at extremely high redshifts.

In this work, we present the first high-precision measurement of C/O for a galaxy at $z = 6.23$ enabled by JWST/NIRSpec measurements of the rest-UV C III], C IV, and O III] lines from the GLASS–JWST ERS program (Treu et al. 2022). This target (source ID 150008 in the GLASS NIRSpec target catalog and ID 2649 in the Stage 1 photometric catalog described by Paris et al. 2023; R.A., decl. = 3.6025240, −30°.4192187) was originally included in the NIRSpec observations as a candidate $z > 5$ galaxy based on photometry indicating a Lyman break. We visually inspected the GLASS–JWST spectra of known candidate $z > 5$ sources for suitability of C/O abundance measurements and selected this as the best example based on clear detection of the necessary rest-UV lines. For many otherwise promising galaxies, either the C III] or O III] lines are not covered due to their position on the slitmask (including the $z \sim 8$ protocluster members described in Morishita et al. 2023). Our current work represents a high-redshift case study which also serves to illustrate the value and feasibility of a future enlarged sample.

This paper is organized as follows. In Section 2 we describe the observations, data reduction, and photometric and spectroscopic measurements. In Section 3 we derive the physical properties of this target, including the electron temperature (Section 3.1), ionic and total abundance ratios (Section 3.2), and stellar population properties (Section 3.3). We discuss the results and present our conclusions in Section 4.

Throughout this work we adopt the concordance ΛCDM cosmology with $H_0 = 70$ km s^{-1} Mpc^{-1}, $\Omega_m = 0.3$, and $\Omega_\Lambda = 0.7$. We use atomic data from Tayal & Zatsarinny (2017) for O^{++} collision strengths, Froese Fischer & Tachiev (2004) for O^{++} transition probabilities, Berrington et al. (1985) for C^{++} collision strengths, Aggarwal & Keenan (2004) for C^{3+} collision strengths, and Wiese et al. (1996) for C^{++} and C^{3+} transition probabilities. We adopt the solar abundance pattern of Asplund et al. (2021).

2. Observations

2.1. Photometry

We use seven-band JWST/NIRCam photometry from the UNCOVER program (JWST-GO-2561; Bezanson et al. 2022) to constrain the stellar population and SFH. The data reduction and measurement methods are as described in Merlin et al. (2022) and Paris et al. (2023); here we give a brief summary. The mosaics in all bands are obtained using a customised version of the STScI pipeline for JWST (CRDS_VER 11.16.14, CAL_VER 1.8.2), with tailored modules to accurately perform the astrometric alignment and to remove defects such as snowballs, wisps, and claws (see Rigby et al. 2023). Sources are detected on the F444W image using SEXTRACTOR (Bertin & Arnouts 1996). To extract the multiband photometry, images from each photometric filter are first convolved to match the F444W filter's point-spread function. Colors are then measured within an 0.″28 circular aperture (twice the FWHM of the F444W image) using A-PHOT (Merlin et al. 2019). The total F444W flux is calculated within a Kron elliptical aperture, with fluxes in other bands given by the 0.″28-aperture color scaled to the total flux. The results are given in Table 1.

At the redshift $z = 6.23$ of our target, F356W and F444W broadband fluxes include strong nebular emission lines (Hβ+[O III] and Hα, respectively). This is clearly apparent in the photometry (Table 1), with flux density in these bands elevated by a factor ∼1.5. The difference of ∼0.07 μJy in F356W compared to adjacent filters suggests approximately 1.3×10^{-17} erg s^{-1} cm^{-2} of emission line flux contribution, in reasonable agreement (within ∼10%) with the measured fluxes of [O III] and Hβ (Section 2.2). The F410M filter is relatively unaffected by nebular emission and provides a reliable measurement of stellar continuum at rest-frame ∼5700 Å. Overall the NIRCam photometry provides good sampling of the rest-frame UV through optical continuum (≃1400–7000 Å) including the Balmer and 4000 Å breaks. We additionally include fluxes from the Hubble Space Telescope (HST) via the Frontier Fields program (Castellano et al. 2016; Merlin et al.

Table 1
Emission Line Fluxes and Photometry

Transition	Flux (10^{-18} erg s^{-1} cm^{-2})	FWHM (Å)
[O III] λ5007[a]	9.53 ± 0.08	16.4 ± 0.2
Hβ[a]	1.71 ± 0.07	
Hδ	0.38 ± 0.05	12.2 ± 1.9
C III] λ1909[b]	0.20 ± 0.05	
C III] λ1907[b]	0.36 ± 0.06	5.3 ± 0.9
O III] λ1666[c]	0.53 ± 0.08	8.3 ± 1.4
He II λ1640[c]	0.09 ± 0.07	
C IV λ1551[d]	0.22 ± 0.06	
C IV λ1549[d]	0.23 ± 0.06	4.5 ± 1.1
Filter	f_ν (μJy)	
F435W	0.001 ± 0.002	
F606W	0.001 ± 0.003	
F814W	0.016 ± 0.002	
F105W	0.113 ± 0.027	
F125W	0.110 ± 0.024	
F160W	0.091 ± 0.031	
F115W	0.106 ± 0.005	
F150W	0.109 ± 0.004	
F200W	0.118 ± 0.004	
F277W	0.109 ± 0.003	
F356W	0.179 ± 0.003	
F410M	0.113 ± 0.005	
F444W	0.172 ± 0.008	

Notes. Line widths are given as the FWHM from Gaussian fits with no correction for the instrument line spread function. In cases where multiple lines are fit jointly (with the same width and redshift), the FWHM is reported only for the strongest line. Photometric flux densities f_ν are measured following the methods described in Merlin et al. (2022) and Paris et al. (2023). The top measurements in filters F435W through F160W are from HST, while F115W and below are from JWST/NIRCam.
[a] Joint fit of [O III] $\lambda\lambda$4959,5007 and Hβ.
[b] Joint fit of C III] $\lambda\lambda$1907,1909.
[c] Joint fit of O III] $\lambda\lambda$1661,1666 and He II λ1640.
[d] Joint fit of C IV $\lambda\lambda$1549,1551.

2016; Lotz et al. 2017; data are available in MAST:10.17909/t9-4xvp-7s45) which sample across the Lyman break at $z = 6.23$. However, the HST photometry has little effect on results in this paper.

2.2. NIRSpec Spectroscopy and Line Fluxes

We obtained moderate resolution ($R = \lambda/\Delta\lambda \simeq 2700$) spectroscopy covering $\lambda_{\rm obs} \simeq 1.0$–$5.3\,\mu$m with JWST/NIRSpec in multi-object spectroscopy mode as part of the GLASS–JWST survey (ERS 1324, PI Treu; Treu et al. 2022; see also Morishita et al. 2023 for details of the NIRSpec observations). The slitlet position for our target is shown in Figure 1. We reduced the NIRSpec spectra using a combination of the default STScI JWST calibration pipeline and the MSAEXP software.[23] First, count-rate maps are produced from the uncalibrated data using CALWEBB_DETECTOR1 with the most recent available reference files (JWST_1014.PMAP). Then MSAEXP conducts additional preprocessing steps to remove the 1/f noise and "snowball" features in the rate images, and calls the level-2 CALWEBB_SPEC2 reduction scripts to extract 2D spectra from individual exposures, after WCS registration, slit path-loss correction, flat-fielding, wavelength and flux calibrations. Subsequently, MSAEXP performs an optimal 1D spectral extraction based on the Horne (1986) algorithm, utilizing the target light profile along the cross-dispersion direction for the optimal extraction aperture. Finally, the 1D spectra extracted from multiple exposures at various dither positions and visits are combined via median stacking with outlier rejections. Our target has well-detected continuum traces in individual exposures, making it feasible to extract and combine the 1D spectra as opposed to first combining the 2D spectra. This method is advantageous for bright objects with sub-pixel dithering, since it enables oversampling the line spread function of our NIRSpec observations in order to improve the sampling of the emission line profiles.

Given the location of our target on the slitmask, the observed wavelength coverage is approximately 1.0–1.6 μm with F100LP/G140H, 1.7–2.65 μm with F170LP/G235H, and 2.9–4.5 μm with F290LP/G395H. There is also a $\sim$0.1 μm detector gap near the short-wavelength end of each range. This range corresponds to $\sim$1360–6220 Å in the rest frame. The spectra include several key rest-frame UV lines used in this analysis (C III] $\lambda\lambda$1907,1909, O III] $\lambda\lambda$1661,1666, C IV $\lambda\lambda$1549,1551) as well as prominent rest-frame optical lines (Hδ, Hβ, [O III] $\lambda\lambda$4959,5007), shown in Figure 1. Hγ and [O III] λ4363 are not covered due to the detector gap, while Hα and [O II] $\lambda\lambda$3727,3729 fall redward of the detector area for the slitmask position. Although these missing lines would be useful, the available spectral coverage is suitable for our goal of measuring the C/O abundance.

To account for uncertainties in flux calibration, slit loss, or other factors, we scale the observed spectra to match the photometric flux densities (Section 2.1). The median spectroscopic continuum value is measured within 0.05 μm of the central wavelength for F150W (for the G140H spectrum), 0.07 μm for F200W (G235H spectrum), and 0.10 μm for F410M (G395 spectrum). These filters and spectral ranges are chosen to sample representative parts of each spectral tuning, avoiding strong emission lines. The resulting signal-to-noise is $\gtrsim$20 in the median continuum values. The spectra from each grating are then scaled such that these median flux densities match the photometric measurements (Table 1). Notably the main result of C/O abundance derived in this paper is relatively unaffected by scaling effects such as flux calibration and slit losses, since the relevant rest-frame UV lines are close in wavelength and observed in the same grating (F100LP/G140H).

Each emission line of interest is fit with a Gaussian profile along with a first-order polynomial to model the continuum, within a range $\Delta\lambda \simeq 0.1$ μm around the line centroid. The best-fit line fluxes and Gaussian full width at half maximum (FWHM) values are given in Table 1, with line profiles shown in Figure 1. We fit nearby lines jointly, such as the UV emission doublets and the optical [O III]+Hβ, using the same redshift and Gaussian width for each line. We also impose the theoretically expected flux ratios [O III] $\lambda5007/\lambda4959 = 2.98$ and O III] $\lambda1666/\lambda1661 = 2.49$ in these joint fits, and we report only the stronger line of each doublet. We do not impose constraints on the C IV doublet flux ratio as it can be affected by resonant absorption and scattering, as well as P Cygni stellar features.

In general we find that residuals from these fits are consistent with the noise level. The sole exception is the optical [O III]

[23] https://github.com/gbrammer/msaexp

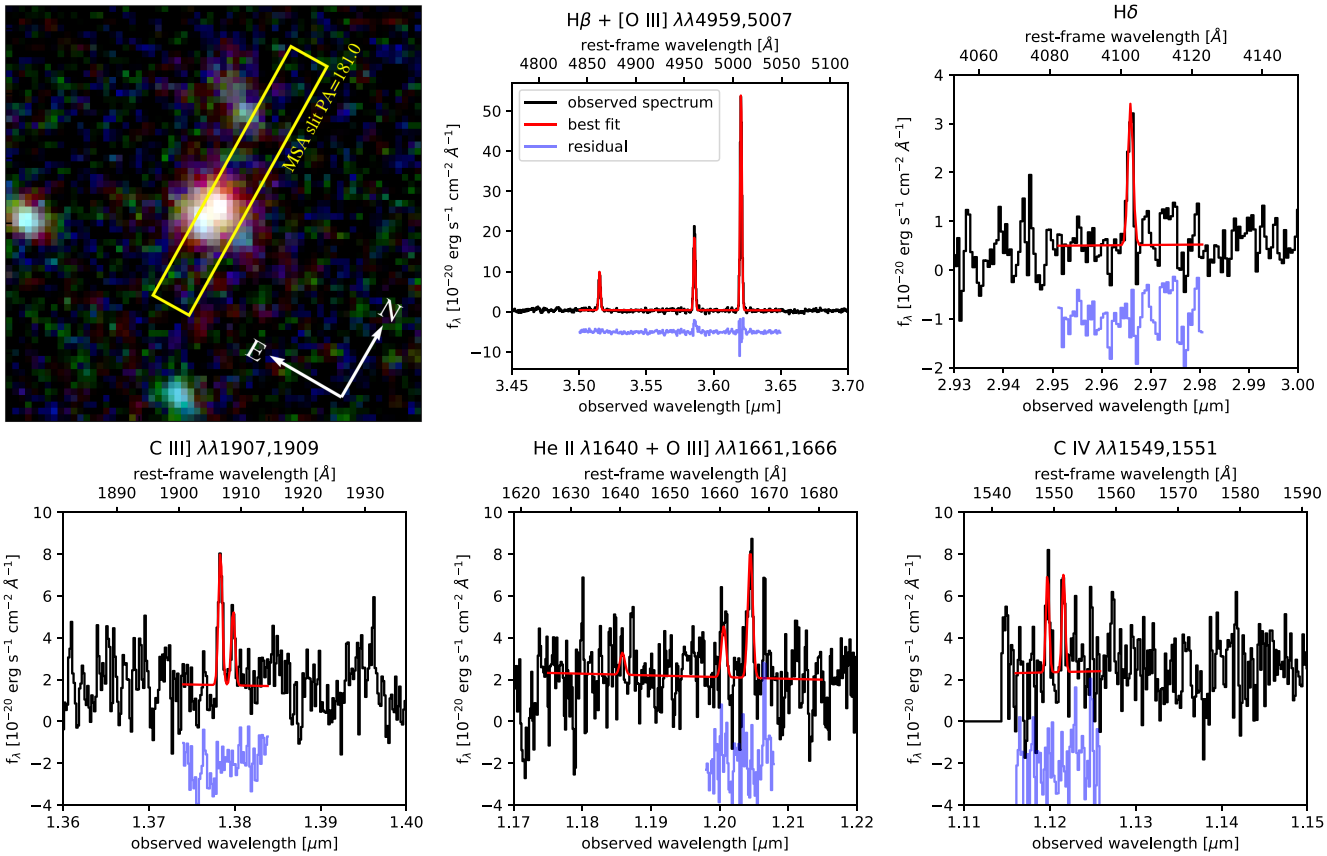

Figure 1. Overview of the spectroscopic data. The top left panel shows JWST/NIRCam imaging (F115W/F200W/F444W = blue/green/red) in a $2'' \times 2''$ field centered on the target galaxy, with the position of the NIRSpec slitlet indicated by the rectangle. The other panels show regions of the spectra around the main emission lines used in this work with best-fit profiles shown in red (see Section 2.2 for details). Residuals around each line are shown in blue, offset vertically for clarity. All key lines used in this work are clearly detected, with $\gtrsim 7\sigma$ significance for the rest-UV O III] and C III] doublets and 5.2σ for the C IV doublet. Residuals are generally consistent with the noise level in the spectra, except for [O III] $\lambda\lambda$4959,5007 which is discussed in Section 2.2.

doublet, for which the joint fit underestimates the flux of [O III] λ4959 by 15% (and overestimates [O III] λ5007 by 2%) compared to fitting the lines individually. Given this disagreement with the expected flux ratio, the true uncertainty in [O III] λ5007 flux may be as large as $\sim$10% (in contrast to the $\sim$1% statistical uncertainty reported in Table 1). However, even if all lines in our analysis are subject to an additional 10% uncertainty in flux, this would still be comparable to or smaller than the statistical uncertainty in derived physical properties.

The redshifts of each line fit provide a useful check of the wavelength calibration and uncertainty estimates. Excluding C IV, the remaining four independent fits are all consistent within 1σ of their weighted mean $\bar{z} = 6.22895 \pm 0.00007$ (with $\chi^2 = \sum \frac{(z-\bar{z})^2}{\sigma_z^2} = 1.6$ for 3 degrees of freedom). This indicates a reliable wavelength scale and good fitting results. We exclude C IV emission from this mean because it shows a clear redward velocity shift of 171 ± 14 km s^{-1} relative to $\bar{z}$ (Figure 2). The C IV emission appears to be real, exhibiting two lines (both at $>3\sigma$) at the expected doublet separation with $>5\sigma$ combined significance in our joint fit. We interpret this shift as arising from scattering in a galactic-scale outflow, which produces the commonly observed redshifted emission in resonant lines (such as C IV, Mg II, and Lyα; e.g., Prochaska et al. 2011). In this scenario we also expect C IV absorption at velocities $v \lesssim 0$ from interstellar and outflowing gas along the line of sight. Consequently the C IV emission flux can be affected by such absorption (as described in detail by, e.g., Senchyna et al. 2022). However, the continuum signal-to-noise is such that we cannot obtain constraining measurements of interstellar absorption. Similarly we do not have strong constraints on the stellar P Cygni component, which can also affect the nebular emission line profile.

We additionally consider the line widths as a test of the fit quality and as a dynamical mass estimator. The instrument resolution is FWHM $\simeq$14.7 Å in G395H (corresponding to Hδ, Hβ, and [O III]) and 5.2 Å in G140H (C IV, C III], O III]). The only fit with FWHM $>3\sigma$ above the instrument resolution is for Hβ and [O III], which gives an intrinsic velocity FWHM $= 60 \pm 4$ km s^{-1} corrected for the instrument resolution. All other fits agree within 2σ of this value, including Hδ and C IV whose best-fit FWHMs are smaller than the instrument resolution. For He II λ1640, the line width is fit jointly with O III] and the resulting fit should thus be interpreted as a nebular component (as opposed to, e.g., broad stellar emission). Regardless, He II emission is not detected ($\sim 1\sigma$). We note that excluding He II from the fit has negligible effect on the derived O III] flux or line width. While we find an intrinsic velocity width FWHM $\simeq$ 60 km s^{-1}, this may be an underestimate since the source appears to not fill the entire slit width (Figure 1). The longer-wavelength lines are likely more accurate as the coarser angular resolution will result in more uniform slit illumination. Our line width measurement is indeed based on the reddest lines available. The implied dynamical mass is $\sim 4 \times 10^8\, M_\odot$ within a radius of 1 kpc, with uncertainty of order a factor of 2 (e.g., Law et al. 2009).

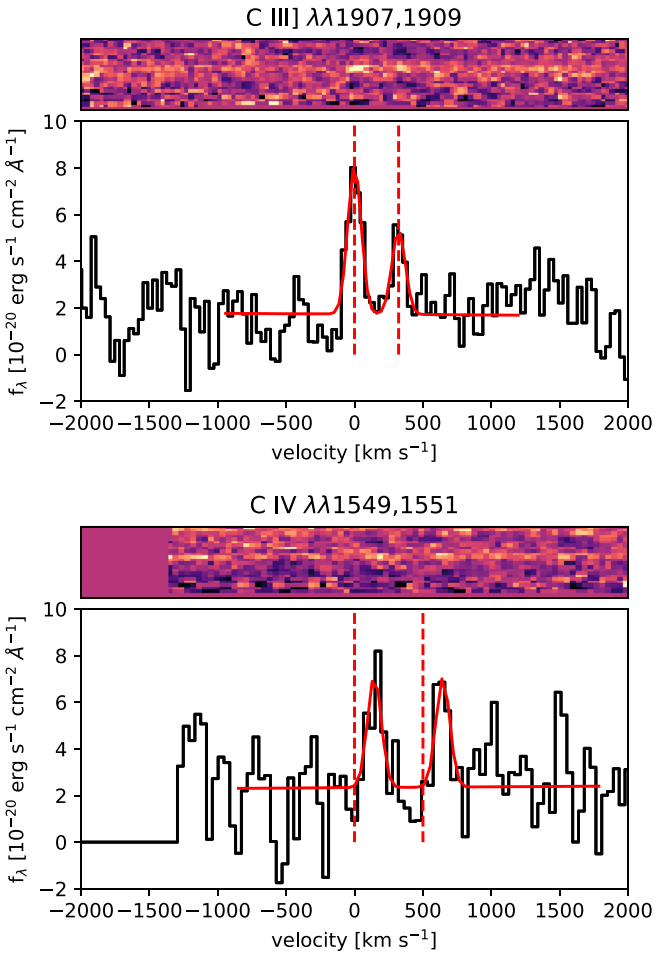

Figure 2. 2D and 1D spectra of rest-frame UV emission lines in velocity space. Vertical dashed lines in the 1D panels show expected line centers for the C III] and C IV doublets, relative to the best-fit redshift of optical [O III] and Hβ. The velocity origin in each panel corresponds to the bluer line. Best-fit line profiles (Section 2.2) are shown in red. The C III] redshift is consistent with the optical lines and rest-UV O III], while C IV emission is redshifted by $\sim$170 km s^{-1}. This C IV velocity offset can be plausibly explained by resonant scattering in a galactic outflow.

3. Physical properties

In this section we present physical properties derived from the photometry and emission line measurements. Quantities such as the stellar mass and star formation rate (SFR) must be corrected for the modest lensing magnification. We adopt a magnification factor $\mu = 2.7 \pm 0.1$ obtained from the lens model described in Bergamini et al. (2023a, 2023b). This value and 1σ confidence interval are determined from a Monte Carlo analysis, and account for the positional accuracy recovered in the updated model (Bergamini et al. 2023b). The formal lensing uncertainties are small and we do not propagate them through the analysis, so that the derived properties can more easily be updated with predictions from other lens models. However, most of the relevant properties for this work (e.g., chemical abundances and stellar population age) are independent of lensing magnification.

3.1. Nebular Reddening, Temperature, and Density

The primary goal of this work is to determine the gas-phase abundances, particularly the C/O ratio. Here we use the direct T_e method which relies on nebular temperature (T_e) and density (n_e) measurements.

Table 2
Physical Properties

Property	Value
RA	00:14:24.607
Decl.	−30:25:09.24
z	6.22895 ± 0.00007
μ	2.7 ± 0.1
log M_* ($M_\odot$)[a]	$8.39^{+0.35}_{-0.19}$
SFR$_{SED}$ ($M_\odot$ yr^{-1})[a]	$5.1^{+6.2}_{-1.1}$
SFR$_{H\beta}$ ($M_\odot$ yr^{-1})	10^{+14}_{-5}
Age$_{par}$ (Myr)[a]	126^{+375}_{-70}
Age$_{non-par}$ (Myr)[b]	99^{+132}_{-63}
$E(B-V)_{gas}$	$0.25^{+0.21}_{-0.18}$
T_e (K)	24300^{+9600}_{-4700}
n_e (cm^{-3})	<8200
Abundances	
$12 + \log(O^{++}/H^+)$	$7.34^{+0.20}_{-0.22}$
$12 + \log(O/H)$[c]	$7.39^{+0.23}_{-0.20}$
$\log(C^{++}/O^{++})$	-1.18 ± 0.11
$[C^{++}/O^{++}]$[d]	-0.95 ± 0.11
$\log(C^{3+}/C^{++})$	-0.33 ± 0.17
$\log\left(\frac{C^{3+}+C^{++}}{O^{++}}\right)$	-1.01 ± 0.12
$\left[\frac{C^{3+}+C^{++}}{O^{++}}\right]$[d]	-0.78 ± 0.12
log(C/O)	-1.01 ± 0.12 (stat) ± 0.15 (sys)

Notes. The stellar mass (M_*) and SFR values are corrected for lensing magnification μ, while other derived properties are not affected by lensing. For ion abundances such as C^{++}/O^{++} we report the statistical uncertainties, excluding systematic uncertainty arising from possible differences in T_e associated with different ions (see the discussion in Section 3.2).
[a] From the parametric SED fitting method of Santini et al. (2023).
[b] From the non-parametric SED fitting method of Morishita et al. (2019).
[c] Assuming O32 is uniformly distributed between 3.0–10 and $T_e(O^+) = T_e(O^{++})$.
[d] Relative to solar $\log(C/O)_\odot = -0.23$ (Asplund et al. 2021).

We first examine the nebular reddening in order to estimate T_e from the [O III] emission lines. The Balmer flux ratio Hδ/Hβ is within 1.4σ of the expected intrinsic value 0.264 (assuming Case B recombination with $T_e = 2 \times 10^4$ K and $n_e = 200$ cm^{-3}). Table 2 lists the reddening $E(B-V) = 0.25^{+0.21}_{-0.18}$ based on the Cardelli et al. (1989) attenuation law with $R_V = 4.05$ (as found by Calzetti et al. 2000). This does not include correction for underlying stellar absorption, which could plausibly reduce the $E(B-V)$ value by $\sim$0.05 based on spectral energy distribution (SED) modeling results (Section 3.3); this is well within the statistical uncertainty. The reddening is insensitive to temperature; an assumed range of $T_e = (1.5-3) \times 10^4$ K results in only ± 0.01 change to $E(B-V)$. We additionally report the SFR derived from reddening-corrected Hβ luminosity using the Kennicutt (1998) calibration corrected to a Chabrier (2003) initial mass function (IMF). While $E(B-V)$ is relatively robust to the choice of attenuation law and R_V, we note that the total attenuation and UV-to-optical correction factor can vary by $\sim$50%. We thus approach the reddening correction cautiously as the uncertainty is fairly large. The SED analyses described in Section 3.3 give best-fitting $E(B-V) = 0.1$–0.3 which, along with the SED-derived SFR,

suggests that the true reddening is likely in the low end of our uncertainty range from $H\delta/H\beta$.

We calculate electron temperature using PYNEB (Luridiana et al. 2015) with the atomic data listed in Section 1. The result is $T_e = 24{,}300^{+9600}_{-4700}$ K from the ratio of UV O III] to optical [O III] emission, using the reddening correction described above (corresponding to a correction factor 2.1× in the UV-to-optical flux ratio) and assuming $n_e = 200\,cm^{-3}$. (The result is insensitive to density; adopting an extreme $10^5\,cm^{-3}$ decreases T_e by only 2000 K.) The uncertainty is entirely dominated by reddening correction, with only ∼1500 K uncertainty from emission line signal-to-noise. We can also place a firm lower limit $T_e > 18{,}000$ K assuming no reddening. While this temperature is much higher than typical nearby galaxies and H II regions (which have $T_e \sim 10{,}000$ K), high T_e is expected in metal-poor and highly star-forming galaxies (e.g., Berg et al. 2021; Pérez-Montero et al. 2021). Indeeed, low-redshift extremely metal-poor galaxies (12+log(O/H) <7.1) have been found with $T_e = 21{,}000$–$25{,}000$ K (e.g., Izotov et al. 2018, 2019, 2021). While such high temperatures may be puzzling given the efficient cooling at $T_e \gtrsim$ 20,000 K, comparable or higher T_e values have been reported in $z > 7$ galaxies based on early JWST observations (e.g., Schaerer et al. 2022; Curti et al. 2023), suggesting they may be common in the rapidly star-forming population at this early epoch.

The C III] doublet ratio is sensitive to electron density. The measured 1907/1909 flux ratio of 1.78 ± 0.47 is compatible with a wide range of densities, though the best-fit measurement is formally unphysical (beyond the low-density limit). The 1σ bounds indicate $n_e < 8200\ cm^{-3}$ assuming $T_e = 24{,}000$ K. We reiterate that the change in derived T_e across this density range is insignificant for our analysis.

3.2. Chemical Abundances

We use the measured line fluxes and physical properties from Section 3.1 to calculate ionic abundances using PYNEB, and report the results in Table 2. Our main interest is C/O. We measure C^{++}/O^{++} ion abundance from the C III] λλ1907, 1909 /O III] λλ1661,1666 flux ratio, which is relatively robust to various sources of uncertainty. The T_e uncertainty propagates to ±0.05 dex in C^{++}/O^{++}, with lower T_e corresponding to lower C^{++}/O^{++} abundance. Flux measurement uncertainty (i.e., signal-to-noise) contributes ±0.06 from each of the O III] and C III] doublets. Considering a range of density $n_e = 1$–$10^3\,cm^{-3}$ corresponds to only ±0.03 dex relative to our assumed $200\,cm^{-3}$ (which is motivated by measurements at $z \gtrsim 2$; e.g., Sanders et al. 2016). Although the high $n_e = 8200\ cm^{-3}$ permitted by our data would increase the derived C/O by 0.08 dex, we also note that C III]-based densities are typically higher than found from the more widely used optical diagnostics (e.g., Mingozzi et al. 2022). Reddening correction is somewhat difficult to assess, as a Milky Way-like attenuation law (e.g., that adopted from Cardelli et al. 1989) indicates that C III] is more attenuated due to the strong 2175 Å "bump" feature, while laws with weak or no bump (e.g., Calzetti et al. 2000; Reddy et al. 2015) instead have larger attenuation of O III]. While the bump feature tends to be weak in metal-poor galaxies, Witstok et al. (2023) have recently reported a Milky Way-like bump strength in a low-metallicity $z \sim 7$ galaxy. We thus conservatively adopt a relative reddening factor of 1.0 ± 0.1 (i.e., within 10% of no reddening) for the O III]/C III] ratio, which encompasses the plausible range of attenuation laws given the $E(B-V)$ value. This corresponds to uncertainty of only ±0.04 dex, relatively small thanks to the small wavelength separation of the rest-UV emission lines. Collectively the total ion abundance uncertainty from sources discussed above is ±0.11 dex, with the largest contribution from signal-to-noise of the rest-UV lines.

Another source of uncertainty is the *relative* temperature associated with C III] and O III] emission, which is not well established, especially at the high T_e of our target. We specifically consider how abundance measurements are affected if C III] is associated with an intermediate-ionization zone characterized by $T_e(S^{++})$, instead of $T_e(O^{++})$. Extrapolating the T_e-T_e relation of Garnett (1992) gives an intermediate-ionization temperature lower by ∼2400 K, propagating to higher C^{++}/O^{++} abundance (although Garnett suggests $T_e(O^{++})$ is more appropriate for C III] emission). In contrast the Croxall et al. (2016) and Rogers et al. (2021) relations suggest the opposite with lower inferred C^{++}/O^{++}. Given these relations, we consider a systematic uncertainty corresponding to ±2400 K difference in $T_e(C^{++})$ relative to $T_e(O^{++})$. This propagates to ±0.15 dex in C^{++} abundance relative to O^{++} and C^{3+}. The magnitude of this effect is therefore potentially comparable to the statistical uncertainties reported in Table 2.

The ratio of C IV/C III] emission allows a measurement of C^{3+}/C^{++} abundance which is useful for assessing ionization correction factors. We assume that the C IV emission is nebular in origin, noting that interstellar absorption or stellar emission can result in under- or over-estimates of the C^{3+} abundance, respectively. Ultimately our reported results allow for up to a conservative factor of 2 uncertainty in C^{3+}. We follow the same approach as for C^{++}/O^{++}, assuming the same temperature in the C^{3+} zone and a relative reddening correction of 1.03 ± 0.10 (i.e., C IV attenuated by 1.03× more than O III] and C III]). The abundance from C IV λ1549 flux is half that from λ1551, although consistent within 1.3σ. We view the λ1551 line as more reliable since it is less susceptible to absorption by interstellar and outflowing gas, and adopt this as our reference for the abundance. The resulting C^{3+}/C^{++} abundance is given in Table 2 with uncertainties propagated as above.

Our best measurement of metal ion abundance relative to hydrogen is O^{++}/H^+, which we obtain from the ratio of [O III] λ5007/Hβ using the T_e method. We report the value as $12 + \log(O^{++}/H^+)$ in Table 2. The uncertainty is dominated by T_e.

3.2.1. Ionization Correction Factor and Total Gas-phase Abundances

Having established the ionic abundances, we now turn to the total gas-phase abundances of C/O and O/H. This requires an ionization correction factor (ICF) for unobserved ions. The ionization correction from O^{++}/H^+ to O/H is typically estimated using the reddening-corrected O32 = [O III] λ5007/[O II] λ3727 ratio alongside a relation to convert measured $T_e(O^{++})$ to $T_e(O^+)$. Since [O II] λ3727 is not covered due to the wavelength range of the observations, we cannot directly measure O32. The [O II] λ2471 line is covered but undetected, yielding a 3σ upper limit of $12+\log(O^+/H^{+}) < 7.35$. This limit suggests that more than half of O is in O^{++}, as expected based on the relatively high C^{3+}/C^{++} ratio. This oxygen ICF (i.e., $O^{++}/O^+ > 1$) in turn suggests an ICF from C^{++}/O^{++} to total C/O of ≳0.75× (e.g., Berg et al. 2019). As this result is relatively unconstraining, we also consider indirect estimates

for O^+. It has been shown that O32 is strongly correlated with the rest-frame equivalent width of [O III] λ5007 (EW(5007)) over 2.5 orders of magnitude for star-forming galaxies at $z \sim 2$–3 (Tang et al. 2019; Sanders et al. 2020). Using the spectroscopically measured EW(5007) $= 480 \pm 30$ Å, the O32–EW(5007) relation of Sanders et al. (2020) implies O32 = 3.6. However, it is unclear whether this relation evolves between $z \sim 2$ and $z > 6$. The handful of published $z > 6$ sources with O32 and EW(5007) measurements (e.g., Schaerer et al. 2022; Trussler et al. 2023; Curti et al. 2023) lie 0.1–0.3 dex above the Sanders et al. (2020) relation, suggesting O32 = 3.6 is a lower limit. The target of this analysis has [O III] $\lambda5007/H\beta = 5.4$, within the range measured by Curti et al. (2023) for three galaxies at $z = 7.5$–8.5 ([O III] $\lambda5007/H\beta = [3.08, 8.29, 7.11]$). These galaxies have O32 = [9.32, 8.94, 13.65],[24] suggesting that O32 of our target falls in a similar range.

To estimate O^+/H^+, we conservatively assume a uniform distribution of O32 = 3.0–10 and adopt the median value of O32 = 6.5 as our fiducial estimate. We further assume that $T_e(O^+) = T_e(O^{++})$, though the resulting total O/H changes by <0.05 dex if we instead use the conversion of Campbell et al. (1986) or Pilyugin et al. (2009). Under these assumptions, we estimate $12+\log(O^+/H^+) = 6.34^{+0.33}_{-0.24}$. We then calculate the total O abundance under the common assumption $O/H = \frac{O^{++}+O^+}{H^+}$, finding $12+\log(O/H) = 7.39^{+0.23}_{-0.20}$. The contribution from O^{3+} is likely negligible in this case (and in all but the most extreme high-ionization sources). Berg et al. (2018) used photoionization modeling to estimate an O^{3+} fraction ≈0.05 for a high-ionization $z \sim 2$ galaxy with $C^{3+}/C^{++} = 0.86$ (see 0.5 ± 0.2 in this work). The non-detection of He II also implies little O^{3+}. Here, a ⩽5% correction for O^{3+} is significantly smaller than other sources of uncertainty.

Our target shows a significant contribution of both C^{++} and C^{3+}, which provides useful information on the likely abundance of other ionic species of C. Photoionization models which reproduce this value of C^{3+}/C^{++}(e.g., Berg et al. 2019) require high-ionization parameters ($\log(U) \sim -1.5$) and low metallicity (≲0.1–0.2 × solar). These models indicate small contributions from other carbon ions (≲10% from C^+). Oxygen ions in such cases are dominated by O^{++}, with ≲10% in the singly and triply ionized states consistent with the assumptions for O/H above. Furthermore, in the photoionization models of Berg et al. (2019), C^+/C is nearly equal to O^+/O across the full range of grid points. Therefore we expect that ionic $\frac{C^{3+}+C^{++}}{O^{++}}$ is approximately equal to total C/O abundance, with this approximation likely accurate to significantly better than 10% for the case where neither C^+ nor O^+ is observed.

We estimate that the sources of uncertainty in converting from ionic to total C/O abundance are of order 0.1 dex. The unseen states of C and O are likely of order ∼10% as discussed above. The C^{3+} abundance may be somewhat underestimated due to scattering and C IV interstellar absorption (Section 2.2), although underlying stellar wind emission could instead cause the C^{3+} abundance to be overestimated. A factor of 2 change in C^{3+} abundance corresponds to only 0.10 dex difference in the total $\frac{C^{3+}+C^{++}}{O^{++}}$, which we view as a conservative limit. We therefore report the total C/O abundance in Table 2 as equal to the $\frac{C^{3+}+C^{++}}{O^{++}}$ with an additional systematic uncertainty term. We note that this value corresponds to an ICF from C^{++}/O^{++} to total C/O of 0.17 dex (or a factor 1.5×), mainly driven by the C^{3+} ion which we measure directly. This ICF(C^{++}/O^{++}) value is consistent with the ICF function of Amayo et al. (2021) for models with $O^{++}/O \approx 0.90$–0.95 (see $O^{++}/O = 0.91 \pm 0.03$ based on O32 assumptions). Allowing for a different relative $T_e(C^{++})$ by up to 2400 K (as discussed above) corresponds to ±0.15 dex in C^{++} and ±0.11 dex in C/O. We sum this in quadrature with the ICF uncertainty and report the total systematic uncertainty as 0.15 dex in C/O abundance (Table 2).

In summary, we have assessed various factors which affect the derived abundance patterns. Ultimately the C/O abundance is based primarily on the well-measured C III]/O III] flux ratio (which to rough approximation scales linearly with C/O), combined with an ICF based on C IV/C III].

3.3. Stellar Mass, Age, and SFH from SED Fitting

We fit the SED using the JWST and HST photometry (Table 1; Figure 3) following the methods of Santini et al. (2023), which demonstrated powerful constraints on the stellar mass of high-redshift ($z \gtrsim 7$) galaxies. We assume the Bruzual & Charlot (2003) stellar templates, a delayed-τ SFH, Chabrier (2003) IMF, and Calzetti et al. (2000) extinction law. This extinction law has the same R_V as that adopted for our spectroscopic analysis, while we further allow for a range of UV attenuation curves (e.g., 2175 Å bump strengths) in determining the C/O abundance in Section 3.2. The best-fit stellar mass M_*, SFR, and stellar age are given in Table 2. M_* and SFR are corrected for lensing magnification.

We refer readers to Santini et al. (2023), Dressler et al. (2023), and Whitler et al. (2023), and references therein, for further discussion of the SFH at high redshifts and the uncertainties associated with SED fitting. A main limitation at high redshifts is the availability of long-wavelength photometry, with JWST/NIRCam providing reasonable sampling redward of the Balmer and 4000 Å breaks up to $z \lesssim 7.5$. The SED of our target is sampled with three filters redward of these breaks (Figure 3), including F410M which is relatively free of strong emission lines and thus anchors the continuum flux density at rest-frame ∼5700 Å.

The most relevant stellar population parameter for our abundance analysis is the stellar age. The SED fit with delayed-τ SFH favors a young ≃130 Myr age, though the 1σ confidence interval extends up to 500 Myr (corresponding to $z \simeq 12$). To assess possible systematic uncertainties and better constrain the age, we performed an independent analysis of the same photometry with a non-parametric SFH using the GSF[25] (Morishita et al. 2019) and SEDz* (Dressler et al. 2023) software packages. In brief, GSF fits the observed photometry with a linear combination of stellar population templates of different age bins, generated with the stellar population synthesis code `fsps` (Conroy et al. 2009), where each bin represents a short (∼30 Myr) burst of constant SFR. SEDz* uses a combination of 10 Myr bursts and constant star formation templates, and is specifically designed to obtain SFHs for $z > 5$ galaxies, taking advantage of the fact that their SEDs are largely dominated by class A stars. Figure 3 shows the best-fit SED and star formation history (stellar mass formed

[24] We calculated O32 based on the observed line fluxes from Curti et al. (2023) using the Cardelli et al. (1989) dust curve assumed in this work.

[25] https://github.com/mtakahiro/gsf

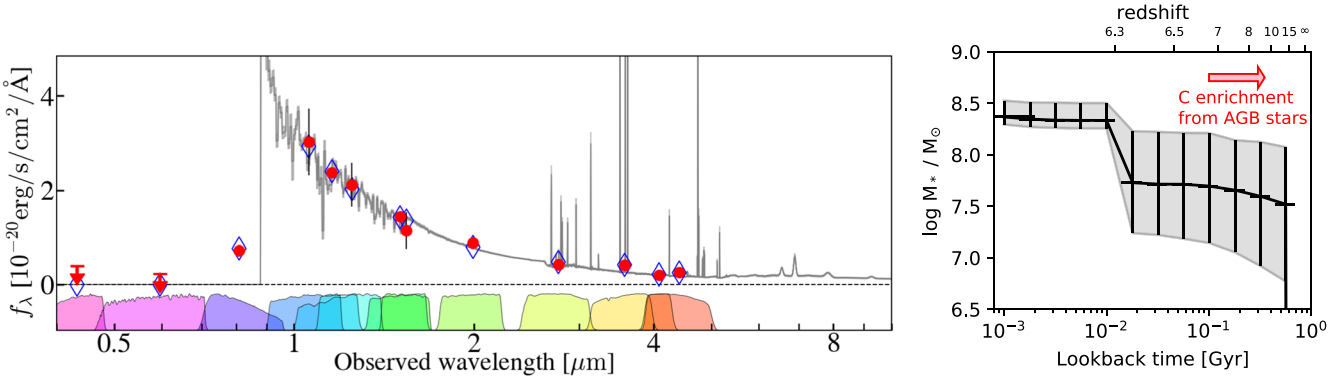

Figure 3. Results of spectral energy distribution (SED) fitting with a non-parametric star formation history (for details see Morishita et al. 2019). Left: the SED fit accurately reproduces the HST and JWST photometry (red points; open diamonds and gray spectrum show the best-fit model results), including strong emission line contributions in the F356W and F444W filters. The filter bandpasses are shown with colored shading below. Right: total stellar mass formed as a function of lookback time, based on the SED fit. The mass shown here is corrected for lensing magnification $\mu = 2.59$ (equivalent to 0.4 dex; we do not propagate the $\sim$1% formal uncertainty in μ here). The $\gtrsim$100 Myr timescale for increased C/O from asymptotic giant branch (AGB) stars is indicated with a red arrow, corresponding to stars formed at $z \gtrsim 7$ in this case. C/O abundance of this galaxy indicates enrichment dominated by core-collapse supernovae (SNe), with a majority of the stars formed within $\lesssim$100 Myr of the observed epoch, consistent with the best-fit mass-weighted age from SED fitting.

per time bin) from GSF. The resulting mass-weighted age of 100^{+130}_{-60} Myr is fully consistent with that following Santini et al. (2023). The de-magnified $\log M_*/M_\odot = 8.37^{+0.16}_{-0.07}$ also agrees within the uncertainties. Likewise, SEDz* fitting results suggest that the majority of stellar mass formed within the preceding $\lesssim$150 Myr. We consider these non-parametric ages to be more reliable. We note that the best-fit stellar population ages are somewhat lower than the predicted average at $z \simeq 6$ from Mason et al. (2015), which could be a result of selection bias for young age arising from the requirement of rest-UV emission line detections. Overall the three separate photometric analyses give a consistent picture but with relatively broad allowed ages, from a few tens to hundreds of Myr. When considering only the photometry, it is thus unclear whether the majority of stars seen in this galaxy formed at $z < 7$ (as indicated by the best-fit ages) or at $z > 8$–10 (allowed within the 1σ bounds). The C/O chemical enrichment information from rest-UV spectroscopy therefore provides a powerful complementary constraint on the SFH.

4. Discussion and Conclusions

We find a low gas-phase abundance ratio $\log(\mathrm{C/O}) = -1.01 \pm 0.12$ (stat) $\pm$ 0.15 (sys) derived primarily from rest-frame UV emission lines. This corresponds to $[\mathrm{C/O}] = -0.78$ relative to the solar scale from Asplund et al. (2021). The overall chemical enrichment of O/H places it near current estimates of the mass–metallicity relation at $z \gtrsim 6$ (e.g., Ma et al. 2016; Jones et al. 2020; Langeroodi et al. 2022), although we caution that this relation is not yet well established at such high redshifts. Figure 4 compares our C/O measurement[26] at $z = 6.23$ with other star-forming galaxies and H II regions at $z \lesssim 3$, the recent $z \approx 8.5$ measurement from Arellano-Córdova et al. (2022), Milky Way stars, and damped Lyα systems measured from quasar spectra. Our measurement is in the lower envelope of known values from previous work, making this galaxy one of the lowest C/O systems known, and comparable to similarly metal-poor galaxies at lower redshifts.

A main point of interest is whether the galaxy is old enough to have undergone significant enrichment from intermediate-mass stars in their AGB phase, as opposed to being dominated by core-collapse SN yields. We calculate the C/O abundance ratio expected from pure core-collapse SN enrichment using values from Nomoto et al. (2013) integrated over the massive end of the IMF, assuming yields for stellar metallicities $Z_* = 0.05$–$0.2\,Z_\odot$ (shaded region in Figure 4). This Z_* range corresponds to adjacent values in the Nomoto et al. (2013) yield tables which straddle the metallicity of our target galaxy. Theoretical yield estimates vary with the initial metallicity which affects, e.g., the stellar evolution, pre-SN mass loss, and rotational velocity. In this case higher initial metallicity results in larger predicted C/O yields. The core-collapse C/O ratio lies at the extreme lower envelope of local and $z \sim 2$ sources, such that the vast majority of known sources require additional enrichment from AGB stars.

Our C/O measurement agrees with the SN yield predictions (Figure 4), indicating minimal carbon enrichment from processes other than massive star SNe. This implies a stellar population age $\lesssim$150 Myr. In older systems, we would expect to see enhanced carbon abundance due to significant enrichment from AGB stars. Including the full yields from AGB stars down to 1 $M_\odot$ (Nomoto et al. 2006) increases the C/O ratio by 0.5–0.6 dex compared to SNe alone, i.e., to $\log(\mathrm{C/O}) = -0.4$ to -0.5 for the same metallicity range shown in Figure 4. Considering only the yields from stars with main-sequence lifetimes shorter than the age of the universe at $z = 6.3$ (i.e., $M_* > 2.5$–$3\,M_\odot$) results in a $\sim$0.25 dex increase to $\log(\mathrm{C/O}) \approx -0.7$. While a 0.25 dex enhancement is compatible with our measurement, this assumes a closed-box chemical evolution with no inflow or outflow. For the closed-box case we can use the oxygen yields ($y_O \approx 0.038$ for the metallicity of our target and our adopted IMF; Vincenzo et al. 2016) to infer a gas fraction $\mu = \frac{M_{\rm gas}}{M_{\rm gas} + M_*} = 0.89 \pm 0.05$. Given the measured stellar mass (Table 2), the resulting total baryonic mass $M \simeq 2.2 \times 10^9\,M_\odot$ is several times larger than the dynamical mass estimated in Section 2.2. This in turn suggests that a majority of the oxygen produced in SNe is ejected via outflows, which can increase C/O relative to the closed-box yields in the case where AGB enrichment has occurred. Incidentally, the redshifted C IV emission (Figure 2; Section 2.2) is indicative of a metal-enriched outflow in our target.

[26] For display purposes we add the statistical and systematic uncertainty in quadrature, giving $\log(\mathrm{C/O}) = -1.01 \pm 0.19$.

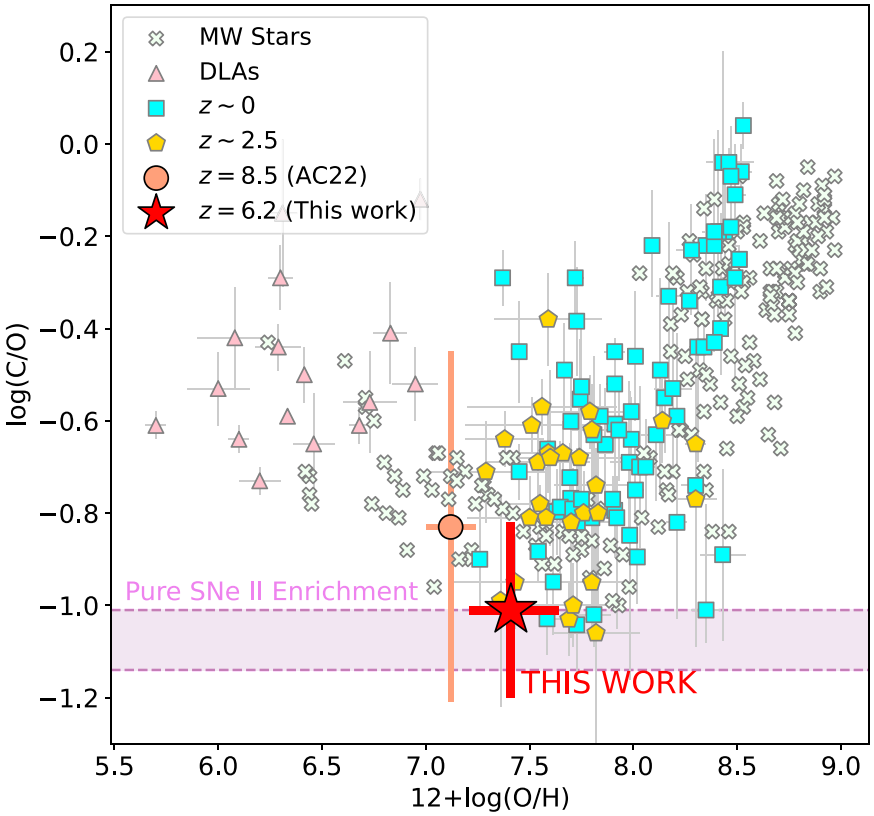

Figure 4. The log(C/O) and 12 + log(O/H) values of our target $z = 6.23$ galaxy (red star) compared to other objects compiled from literature: Milky Way halo and disk stars (light-green crosses; Gustafsson et al. 1999; Akerman et al. 2004; Fabbian et al. 2009; Nissen et al. 2014); damped Lyα absorbers (DLAs; pink triangles; Cooke et al. 2017); local dwarf galaxies (Berg et al. 2016, 2019; Peña-Guerrero et al. 2017; Senchyna et al. 2017); and $z = 0$ H II regions (Tsamis et al. 2003; Esteban et al. 2004, 2009, 2014, 2017; García-Rojas et al. 2004, 2005, 2006; Peimbert et al. 2005; García-Rojas & Esteban 2007; López-Sánchez et al. 2007; Toribio San Cipriano et al. 2016, 2017) ($z \sim 0$; cyan squares); high-redshift galaxies near cosmic noon ($z \simeq 1.5$–3.5) (orange pentagons; Fosbury et al. 2003; Erb et al. 2010; Christensen et al. 2012; Bayliss et al. 2014; James et al. 2014; Stark et al. 2014; Steidel et al. 2016; Vanzella et al. 2016; Amorín et al. 2017; Berg et al. 2018; Mainali et al. 2020; Matthee et al. 2021; Rigby et al. 2021; Iani et al. 2023); and a galaxy at $z = 8.5$ from Arellano-Córdova et al. (2022) (AC22: orange circle). The log(C/O) ratio from pure core-collapse SNe enrichment is marked with violet shading. This C/O range was calculated using the $Z_* = 0.05 Z_\odot$ and $0.2 Z_\odot$ values from the Nomoto et al. (2013) yield tables assuming a Salpeter (1955) initial mass function. The C/O abundance ratio of this galaxy is at the lower envelope of other low-metallicity sources, consistent with pure SNe II enrichment and implying a young stellar population without significant enrichment from AGB stars. Note: for the $z = 0$ H II regions, C/O was measured from recombination lines (RLs). We plot O/H derived using the collisionally excited line (CEL) T_e-method to match the O/H scale of the $z \sim 0$ dwarf galaxy and $z \gtrsim 2$ samples. We assume that the abundance discrepancy factor is the same for C and O (e.g., Toribio San Cipriano et al. 2017), such that C/O derived from RLs and CELs can be fairly compared.

Chemical evolution models clearly indicate that the pure core-collapse "floor" C/O value can only be reached when there is no preferential removal of O relative to C from SNe-driven outflows, which is likely not the case when long-timescale AGB enrichment is present (e.g., Yin et al. 2011; Berg et al. 2019). These models suggest $\log(\mathrm{C/O}) \gtrsim -0.5$ following enrichment from AGB stars when modest outflows are included (e.g., when $\gtrsim$30% of oxygen is ejected). Our results do not support such high C/O values. This conclusion of little AGB contribution—based on chemical abundance analysis—is consistent with the results of SED fitting which likewise indicate a young age, although with large uncertainty (100^{+130}_{-60} Myr; Section 3.3, Figure 3). The $z \approx 8.5$ source with $\log(\mathrm{C/O}) = -0.83 \pm 0.38$ from Arellano-Córdova et al. (2022) is also inferred to have a very young age (<10 Myr; Carnall et al. 2023), and is consistent with the pure core-collapse scenario, though the abundance constraint for this object is not robust due to the larger uncertainty.

Overall our results indicate a picture of rapid buildup of stellar mass in a galaxy seen only ≃900 Myr after the big bang, with the majority of stellar mass assembled since $z \lesssim 8$ (i.e., within 150 Myr) and likely even more recently. The current SFR and stellar mass suggest a mass-doubling timescale of only $\lesssim$50 Myr, indicating a rising star formation history based on SED fitting (Figure 3). It is therefore unlikely that this galaxy would have contributed significantly to cosmic reionization at $z \gtrsim 8$, as our C/O abundance analysis indicates little star formation ($\lesssim 10^8\, M_\odot$ total mass) before this time.

As our results represent the most robust C/O abundance to date in such a high-redshift galaxy, we reflect briefly on lessons learned and prospects for future study. Sensitive rest-UV spectroscopy is essential for this result; the relatively small uncertainty is thanks to clear detection of the UV O III], C III], and C IV emission doublets. Notably, we find that C IV is important for assessing the ionization correction factor in this case (where we find C^{3+} contributes at the level of 0.17 dex), whereas it is often not significant in lower-redshift samples. Care should be taken to assess possible interstellar absorption and stellar contributions to the C IV profile. One of the larger sources of uncertainty is the relative T_e associated with emission lines of different ions, as discussed in Section 3.2, which warrants further examination to reach precision better than ≃0.1 dex. The precision of our measurement could also be improved with the addition of [O II] $\lambda\lambda$3726,3729, not covered

in our observations, which would yield improved estimates of the ICF. The [O II] doublet would also provide a better measurement of electron density n_e. Measurements of rest-optical [O III] λ4363 (falling in the chip gap in our G395H observations) would provide a better constraint on T_e relative to our value based on rest-UV O III] λ1666, for which the error budget is dominated by uncertainty on the reddening correction. The main consequence of these missing emission line diagnostics is that total O/H (and C/H) abundances have larger uncertainty; the effect on derived C/O abundance is relatively minor. Nonetheless it is fully within the capabilities of JWST/NIRSpec to provide these additional measurements with an appropriate mask and filter configuration. Our result thus represents only a lower limit to the C/O precision that can be achieved at $z > 6$ with NIRSpec spectroscopy. There is also room for improvement in chemical evolution modeling, which has largely focused on abundance patterns at lower redshifts (e.g., Yin et al. 2011; Berg et al. 2019; Kobayashi et al. 2020). The results of this work and other high-redshift abundance analyses (e.g., Arellano-Córdova et al. 2022; Cameron et al. 2023) motivate exploring multi-element models which are specifically tailored to the rapid formation histories expected in the first billion years of the universe.

This work demonstrates the value of gas-phase C/O abundance for characterizing SFHs of galaxies in the epoch of reionization, and the feasibility of reaching good precision with JWST data. A larger sample of $z > 6$ targets with C/O measurements will be valuable to characterize the typical SFHs and to compare with complementary results from photometry and SED fitting. For example, Laporte et al. (2023) find stellar population ages >150 Myr in two galaxies at $z > 8$ within a sample of six based on JWST photometry, improving upon earlier Spitzer-based results (e.g., Roberts-Borsani et al. 2020). We would expect these older galaxies to exhibit higher C/O. A positive correlation between C/O and photometrically derived ages (e.g., Dressler et al. 2023) would bolster confidence in both methods. If instead rapid formation histories and ages $\lesssim$150 Myr are a uniform feature of $z > 6$ galaxies, then we expect the population to display lower average C/O and smaller intrinsic scatter in C/O at fixed O/H relative to samples at $z \sim 0$ and $z \sim 2-3$ (Figure 4). Our results motivate the assembly of a larger sample of reionization-era targets with robust rest-UV C III] and O III] measurements to constrain the timescale of galaxy assembly in the early universe.

Acknowledgments

We thank Michael Topping for allowing a comparison of the line fluxes derived in this work to those measured from an independent data reduction. We are grateful to the referee for providing a constructive review which improved this manuscript. This work is based on observations made with the NASA/ESA/CSA James Webb Space Telescope. This work also uses observations made with the NASA/ESA Hubble Space Telescope. The data were obtained from the Mikulski Archive for Space Telescopes at the Space Telescope Science Institute, which is operated by the Association of Universities for Research in Astronomy, Inc., under NASA contract NAS 5-03127 for JWST. The NIRSpec and NIRCam observations are associated with programs JWST-ERS-1324 and JWST-GO-2561, respectively. We acknowledge financial support for program GLASS-JWST ERS-1324 provided by NASA through grant JWST-ERS-1324 from the Space Telescope Science Institute. Support for this work was provided by NASA through the NASA Hubble Fellowship grant HST-HF2-51469.001-A awarded by the Space Telescope Science Institute, which is operated by the Association of Universities for Research in Astronomy, Incorporated, under NASA contract NAS5-26555. We acknowledge support from the INAF Large Grant 2022 "Extragalactic Surveys with JWST" (PI Pentericci). X.W. is supported by CAS Project for Young Scientists in Basic Research, grant No. YSBR-062. M.B. acknowledges support from the Slovenian national research agency ARRS through grant N1-0238. K.G. and T.N. acknowledge support from Australian Research Council Laureate Fellowship FL180100060. The Cosmic Dawn Center is funded by the Danish National Research Foundation (DNRF) under grant #140. Cloud-based data processing and file storage for this work is provided by the AWS Cloud Credits for Research program.

ORCID iDs

Tucker Jones https://orcid.org/0000-0001-5860-3419
Ryan Sanders https://orcid.org/0000-0003-4792-9119
Yuguang Chen https://orcid.org/0000-0003-4520-5395
Xin Wang https://orcid.org/0000-0002-9373-3865
Takahiro Morishita https://orcid.org/0000-0002-8512-1404
Guido Roberts-Borsani https://orcid.org/0000-0002-4140-1367
Tommaso Treu https://orcid.org/0000-0002-8460-0390
Alan Dressler https://orcid.org/0000-0002-6317-0037
Emiliano Merlin https://orcid.org/0000-0001-6870-8900
Diego Paris https://orcid.org/0000-0002-7409-8114
Paola Santini https://orcid.org/0000-0002-9334-8705
Pietro Bergamini https://orcid.org/0000-0003-1383-9414
A. Henry https://orcid.org/0000-0002-6586-4446
Themiya Nanayakkara https://orcid.org/0000-0003-2804-0648
Kristan Boyett https://orcid.org/0000-0003-4109-304X
Marusa Bradac https://orcid.org/0000-0001-5984-0395
Gabriel Brammer https://orcid.org/0000-0003-2680-005X
Antonello Calabró https://orcid.org/0000-0003-2536-1614
Karl Glazebrook https://orcid.org/0000-0002-3254-9044
Kathryn Grasha https://orcid.org/0000-0002-3247-5321
Sara Mascia https://orcid.org/0000-0002-9572-7813
Laura Pentericci https://orcid.org/0000-0001-8940-6768
Michele Trenti https://orcid.org/0000-0001-9391-305X
Benedetta Vulcani https://orcid.org/0000-0003-0980-1499

References

Aggarwal, K. M., & Keenan, F. P. 2004, PhyS, 69, 385
Akerman, C. J., Carigi, L., Nissen, P. E., Pettini, M., & Asplund, M. 2004, A&A, 414, 931
Amayo, A., Delgado-Inglada, G., & Stasińska, G. 2021, MNRAS, 505, 2361
Amorín, R., Fontana, A., Pérez-Montero, E., et al. 2017, NatAs, 1, 0052
Arellano-Córdova, K. Z., Berg, D. A., Chisholm, J., et al. 2022, ApJL, 940, L23
Asplund, M., Amarsi, A. M., & Grevesse, N. 2021, A&A, 653, A141
Bayliss, M. B., Rigby, J. R., Sharon, K., et al. 2014, ApJ, 790, 144
Berg, D. A., Chisholm, J., Erb, D. K., et al. 2021, ApJ, 922, 170
Berg, D. A., Erb, D. K., Auger, M. W., Pettini, M., & Brammer, G. B. 2018, ApJ, 859, 164
Berg, D. A., Erb, D. K., Henry, R. B. C., Skillman, E. D., & McQuinn, K. B. W. 2019, ApJ, 874, 93
Berg, D. A., James, B. L., King, T., et al. 2022, ApJS, 261, 31
Berg, D. A., Skillman, E. D., Henry, R. B. C., Erb, D. K., & Carigi, L. 2016, ApJ, 827, 126

Bergamini, P., Acebron, A., Grillo, C., et al. 2023a, A&A, 670, A60
Bergamini, P., Acebron, A., Grillo, C., et al. 2023b, arXiv:2303.10210
Berrington, K. A., Burke, P. G., Dufton, P. L., & Kingston, A. E. 1985, ADNDT, 33, 195
Bertin, E., & Arnouts, S. 1996, A&AS, 117, 393
Bezanson, R., Labbe, I., Whitaker, K. E., et al. 2022, arXiv:2212.04026
Bruzual, G., & Charlot, S. 2003, MNRAS, 344, 1000
Byler, N., Dalcanton, J. J., Conroy, C., et al. 2018, ApJ, 863, 14
Calzetti, D., Armus, L., Bohlin, R. C., et al. 2000, ApJ, 533, 682
Cameron, A. J., Katz, H., Rey, M. P., & Saxena, A. 2023, MNRAS, 523, 3516
Campbell, A., Terlevich, R., & Melnick, J. 1986, MNRAS, 223, 811
Cardelli, J. A., Clayton, G. C., & Mathis, J. S. 1989, ApJ, 345, 245
Carnall, A. C., Begley, R., McLeod, D. J., et al. 2023, MNRAS, 518, L45
Castellano, M., Amorín, R., Merlin, E., et al. 2016, A&A, 590, A31
Chabrier, G. 2003, PASP, 115, 763
Christensen, L., Laursen, P., Richard, J., et al. 2012, MNRAS, 427, 1973
Conroy, C., Gunn, J. E., & White, M. 2009, ApJ, 699, 486
Cooke, R. J., Pettini, M., & Steidel, C. C. 2017, MNRAS, 467, 802
Croxall, K. V., Pogge, R. W., Berg, D. A., Skillman, E. D., & Moustakas, J. 2016, ApJ, 830, 4
Curti, M., D'Eugenio, F., Carniani, S., et al. 2023, MNRAS, 518, 425
Dressler, A., Vulcani, B., Treu, T., et al. 2023, ApJL, 947, L27
Erb, D. K., Pettini, M., Shapley, A. E., et al. 2010, ApJ, 719, 1168
Esteban, C., Bresolin, F., Peimbert, M., et al. 2009, ApJ, 700, 654
Esteban, C., Fang, X., García-Rojas, J., & Toribio San Cipriano, L. 2017, MNRAS, 471, 987
Esteban, C., García-Rojas, J., Carigi, L., et al. 2014, MNRAS, 443, 624
Esteban, C., Peimbert, M., García-Rojas, J., et al. 2004, MNRAS, 355, 229
Fabbian, D., Nissen, P. E., Asplund, M., Pettini, M., & Akerman, C. 2009, A&A, 500, 1143
Fosbury, R. A. E., Villar-Martín, M., Humphrey, A., et al. 2003, ApJ, 596, 797
Froese Fischer, C., & Tachiev, G. 2004, ADNDT, 87, 1
García-Rojas, J., & Esteban, C. 2007, ApJ, 670, 457
García-Rojas, J., Esteban, C., Peimbert, A., et al. 2005, MNRAS, 362, 301
García-Rojas, J., Esteban, C., Peimbert, M., et al. 2004, ApJS, 153, 501
García-Rojas, J., Esteban, C., Peimbert, M., et al. 2006, MNRAS, 368, 253
Garnett, D. R. 1992, AJ, 103, 1330
Gustafsson, B., Karlsson, T., Olsson, E., Edvardsson, B., & Ryde, N. 1999, A&A, 342, 426
Henry, R. B. C., Edmunds, M. G., & Köppen, J. 2000, ApJ, 541, 660
Horne, K. 1986, PASP, 98, 609
Hutchison, T. A., Papovich, C., Finkelstein, S. L., et al. 2019, ApJ, 879, 70
Iani, E., Zanella, A., Vernet, J., et al. 2023, MNRAS, 518, 5018
Izotov, Y. I., Thuan, T. X., & Guseva, N. G. 2019, MNRAS, 483, 5491
Izotov, Y. I., Thuan, T. X., & Guseva, N. G. 2021, MNRAS, 504, 3996
Izotov, Y. I., Thuan, T. X., Guseva, N. G., & Liss, S. E. 2018, MNRAS, 473, 1956
James, B. L., Pettini, M., Christensen, L., et al. 2014, MNRAS, 440, 1794
Jones, T., Sanders, R., Roberts-Borsani, G., et al. 2020, ApJ, 903, 150
Kennicutt, R. C. J. 1998, ARA&A, 36, 189
Kobayashi, C., Karakas, A. I., & Lugaro, M. 2020, ApJ, 900, 179
Kobayashi, C., Karakas, A. I., & Umeda, H. 2011, MNRAS, 414, 3231
Langeroodi, D., Hjorth, J., Chen, W., et al. 2022, arXiv:2212.02491
Laporte, N., Ellis, R. S., Witten, C. E. C., & Roberts-Borsani, G. 2023, MNRAS, 523, 3018
Law, D. R., Steidel, C. C., Erb, D. K., et al. 2009, ApJ, 697, 2057
López-Sánchez, Á., Esteban, C., García-Rojas, J., Peimbert, M., & Rodríguez, M. 2007, ApJ, 656, 168
Lotz, J. M., Koekemoer, A., Coe, D., et al. 2017, ApJ, 837, 97
Luridiana, V., Morisset, C., & Shaw, R. A. 2015, A&A, 573, A42
Ma, X., Hopkins, P. F., Faucher-Giguère, C.-A., et al. 2016, MNRAS, 456, 2140
Mainali, R., Kollmeier, J. A., Stark, D. P., et al. 2017, ApJL, 836, L14
Mainali, R., Stark, D. P., Tang, M., et al. 2020, MNRAS, 494, 719
Maiolino, R., & Mannucci, F. 2019, A&ARv, 27, 3
Mason, C. A., Trenti, M., & Treu, T. 2015, ApJ, 813, 21
Matteucci, F. 2012, Chemical Evolution of Galaxies, Astronomy and Astrophysics Library (Berlin: Springer)
Matthee, J., Sobral, D., Hayes, M., et al. 2021, MNRAS, 505, 1382
Merlin, E., Amorín, R., Castellano, M., et al. 2016, A&A, 590, A30
Merlin, E., Bonchi, A., Paris, D., et al. 2022, ApJL, 938, L14
Merlin, E., Pilo, S., Fontana, A., et al. 2019, A&A, 622, A169
Mingozzi, M., James, B. L., Arellano-Córdova, K. Z., et al. 2022, ApJ, 939, 110
Morishita, T., Abramson, L. E., Treu, T., et al. 2019, ApJ, 877, 141
Morishita, T., Roberts-Borsani, G., Treu, T., et al. 2023, ApJL, 947, L24
Nissen, P. E., Chen, Y. Q., Carigi, L., Schuster, W. J., & Zhao, G. 2014, A&A, 568, A25
Nomoto, K., Kobayashi, C., & Tominaga, N. 2013, ARA&A, 51, 457
Nomoto, K., Tominaga, N., Umeda, H., Kobayashi, C., & Maeda, K. 2006, NuPhA, 777, 424
Paris, D., Merlin, E., Fontana, A., et al. 2023, arXiv:2301.02179
Peimbert, A., Peimbert, M., & Ruiz, M. T. 2005, ApJ, 634, 1056
Peña-Guerrero, M. A., Leitherer, C., de Mink, S., Wofford, A., & Kewley, L. 2017, ApJ, 847, 107
Pérez-Montero, E., Amorín, R., Sánchez Almeida, J., et al. 2021, MNRAS, 504, 1237
Pilyugin, L. S., Mattsson, L., Vílchez, J. M., & Cedrés, B. 2009, MNRAS, 398, 485
Prochaska, J. X., Kasen, D., & Rubin, K. 2011, ApJ, 734, 24
Reddy, N. A., Kriek, M., Shapley, A. E., et al. 2015, ApJ, 806, 259
Rigby, J., Perrin, M., McElwain, M., et al. 2023, PASP, 135, 048001
Rigby, J. R., Florian, M., Acharyya, A., et al. 2021, ApJ, 908, 154
Roberts-Borsani, G. W., Ellis, R. S., & Laporte, N. 2020, MNRAS, 497, 3440
Rogers, N. S. J., Skillman, E. D., Pogge, R. W., et al. 2021, ApJ, 915, 21
Salpeter, E. E. 1955, ApJ, 121, 161
Sanders, R. L., Shapley, A. E., Kriek, M., et al. 2016, ApJ, 816, 23
Sanders, R. L., Shapley, A. E., Reddy, N. A., et al. 2020, MNRAS, 491, 1427
Santini, P., Fontana, A., Castellano, M., et al. 2023, ApJL, 942, L27
Schaerer, D., Marques-Chaves, R., Barrufet, L., et al. 2022, A&A, 665, L4
Senchyna, P., Stark, D. P., Charlot, S., et al. 2022, ApJ, 930, 105
Senchyna, P., Stark, D. P., Vidal-García, A., et al. 2017, MNRAS, 472, 2608
Stark, D. P., Ellis, R. S., Charlot, S., et al. 2017, MNRAS, 464, 469
Stark, D. P., Richard, J., Charlot, S., et al. 2015a, MNRAS, 450, 1846
Stark, D. P., Richard, J., Siana, B., et al. 2014, MNRAS, 445, 3200
Stark, D. P., Walth, G., Charlot, S., et al. 2015b, MNRAS, 454, 1393
Steidel, C. C., Strom, A. L., Pettini, M., et al. 2016, ApJ, 826, 159
Tang, M., Stark, D. P., Chevallard, J., & Charlot, S. 2019, MNRAS, 489, 2572
Tayal, S. S., & Zatsarinny, O. 2017, ApJ, 850, 147
Toribio San Cipriano, L., Domínguez-Guzmán, G., Esteban, C., et al. 2017, MNRAS, 467, 3759
Toribio San Cipriano, L., García-Rojas, J., Esteban, C., Bresolin, F., & Peimbert, M. 2016, MNRAS, 458, 1866
Treu, T., Roberts-Borsani, G., Bradac, M., et al. 2022, ApJ, 935, 110
Trussler, J. A. A., Adams, N. J., Conselice, C. J., et al. 2023, MNRAS, 523, 3424
Tsamis, Y. G., Barlow, M. J., Liu, X. W., Danziger, I. J., & Storey, P. J. 2003, MNRAS, 338, 687
Vanzella, E., De Barros, S., Cupani, G., et al. 2016, ApJL, 821, L27
Vincenzo, F., Matteucci, F., Belfiore, F., & Maiolino, R. 2016, MNRAS, 455, 4183
Whitler, L., Stark, D. P., Endsley, R., et al. 2023, MNRAS, 519, 5859
Wiese, W. L., Fuhr, J. R., & Deters, T. M. 1996, in Atomic Transition Probabilities of Carbon, Nitrogen, and Oxygen : a Critical Data Compilation, ed. W. L. Wiese, J. R. Fuhr, & T. M. Deters (Washington, DC: American Chemical Society)
Witstok, J., Shivaei, I., Smit, R., et al. 2023, arXiv:2302.05468
Yin, J., Matteucci, F., & Vladilo, G. 2011, A&A, 531, A136